Generation of high-flux hyperentangled photon pairs using a microstructure-fiber Sagnac interferometer

Jun Chen,* Jingyun Fan,† Matthew D. Eisaman, and Alan Migdall
Optical Technology Division, National Institute of Standards and Technology, 100 Bureau Drive, Gaithersburg, Maryland 20899-8441, USA
and Joint Quantum Institute, University of Maryland, College Park, Maryland 20742, USA
(Received 19 December 2007; published 15 May 2008)

We demonstrate generation of hyperentangled (time-bin and polarization) photon pairs via four-wave mixing in a microstructure-fiber Sagnac interferometer. The two-photon interference visibility in the time-bin (polarization) degree of freedom is $88\% \pm 2\%$ ($84\% \pm 1\%$) without subtraction of accidental coincidences, and Bell's inequality is violated by 27 standard deviations at a 1 kHz coincidence rate.

DOI: 10.1103/PhysRevA.77.053812 PACS number(s): 42.65.Lm, 42.50.Dv, 03.65.Ud, 03.67.Hk

Entangled photons, essential to many quantum-communication and quantum-cryptography protocols, are now routinely generated in laboratories around the world. Recent experiments [1–4] have produced photons that are simultaneously entangled in more than one degree of freedom, a property referred to as hyperentanglement [5]. Additional information provided by entanglement in extra degree(s) of freedom when two hyperentangled photons are superposed makes it possible to completely distinguish all four Bell states in one degree of freedom with only linear optical elements, a task that is impossible to perform with photons entangled only in one degree of freedom [6]. Previous experimental demonstrations of hyperentangled photons all utilized spontaneous parametric down conversion in second-order ($\chi^{(2)}$) nonlinear crystals [7]. However the typical multimode spatial profiles of these down-converted photons are such that it is difficult to couple them into single-mode optical fibers with low loss, hindering their application in existing fiber-optic networks. Here we demonstrate the generation of photon pairs hyperentangled in both time-bin and polarization degrees of freedom, produced via $\chi^{(3)}$ four-wave mixing in a polarization-maintaining, single-mode microstructure fiber. To our knowledge, this is the first demonstration of hyperentanglement using this type of source, and also the first demonstration of hyperentanglement using polarization and time-bin degrees of freedom. The photons emitted by the microstructure fiber have a high coupling efficiency into standard single-mode fiber, since the two kinds of fiber have compatible spatial-mode profiles [8]. Our hyperentangled photon source is wavelength tunable over 20 nm, exhibits high two-photon interference visibility ($>84\%$) for both degrees of freedom, and is spectrally bright, with a coincidence rate of around 1 kHz at 220 μWof average pump power per 0.9 nm collection bandwidths. These properties make our source potentially useful for many quantum-information-processing applications.

Quantum-correlated, as well as polarization-entangled, photon-pair generation has been demonstrated in both microstructure fiber [9–11] and dispersion-shifted fiber [12–15]. The responsible physical mechanism is four-wave mixing (FWM), in which two pump photons scatter through the Kerr ($\chi^{(3)}$) nonlinearity of an optical fiber to give birth to a pair of daughter photons, commonly denoted as signal and idler. Energy conservation ($2\omega_p = \omega_s + \omega_i$) and momentum conservation ($2\vec{k}_p = \vec{k}_s + \vec{k}_i$) are obeyed during the FWM process, where ω_j and $\vec{k}_j$ stand for the frequency and wave vector of the jth photon, and the subscripts p, s, and i denote the pump, the signal, and the idler photons, respectively. Various polarization-entanglement schemes have been proposed and demonstrated for photon pairs generated using dispersion-shifted fiber [16], while more recently have researchers been able to demonstrate polarization entanglement using microstructure fiber [17,18]. Spontaneous Raman scattering, the predominant process accompanying FWM in optical fibers that generates uncorrelated noise photons, is suppressed either by cooling the fiber down to liquid-nitrogen temperature in the case of dispersion-shifted fiber [15,19], or in the microstructure-fiber case, by careful phase matching of FWM (e.g., by pumping in the normal dispersion regime of the fiber) so that the frequencies of correlated photon pairs are outside of the primary Raman band [11,17].

Time-bin entanglement [20] has also been extensively studied, not only because it is a discrete version of the more well-known time-energy entanglement [21], but also because of its practical advantage of immunity to polarization-mode dispersion in long-distance distribution using optical fibers [22,23]. Methods have been proposed to *convert* polarization entanglement into time-bin entanglement, and vice versa [24]. Here we focus on how to *combine* the two types of entanglement into one hyperentangled state (i.e., photons that are both polarization and time-bin entangled), a task that requires precise spatiotemporal mode matching. Our adoption of a single spatial-mode microstructure fiber in a Sagnac-loop configuration makes the otherwise difficult task of mode matching easier to handle, as will be explained later in more detail. The microstructure fiber's high nonlinearity (its nonlinear parameter [25] $\gamma = 70\ \mathrm{W}^{-1}\,\mathrm{km}^{-1}$) greatly reduces the required amount of pump power, permits us to use a short length fiber (1.8 m in our case), and is the key element in obtaining a photon source with high spectral brightness over a large wavelength range.

Our experimental setup is shown in Fig. 1. The initial

*junchen@nist.gov
†jfan@nist.gov

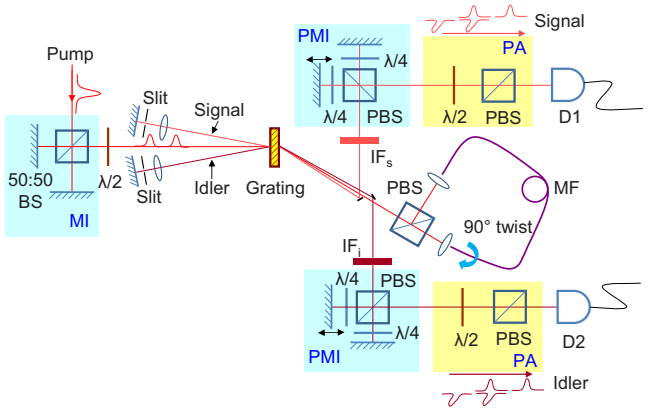

FIG. 1. (Color online) A schematic of the experimental setup. BS, beam splitter; PBS, polarization beam splitter; MF, microstructure fiber; λ/2, half-wave plate; λ/4, quarter-wave plate; IF, interference filter; PA, polarization analyzer; (P)MI, (polarization) Michelson interferometer.

pump pulse (8 ps in duration, 76 MHz repetition rate) is obtained from a Ti-Sapphire laser. The pump central wavelength (λ_p=740.6 nm) is judiciously chosen to be in the normal dispersion regime of the microstructure fiber used in the experiment (the manufacturer-specified zero-dispersion wavelength of the fiber is 745 nm ± 5 nm), so that the phase-matched FWM sidebands lie outside of the primary Raman band (peaked at 13 THz, or in our case, 23.7 nm detuned from the pump). The pump pulse is then split into two identical pump pulses by passing it through an unbalanced Michelson interferometer (MI in Fig. 1), which is constructed with a 50:50 beam splitter (BS) and two mirrors to provide a delay of $\Delta\tau$=57 ps between the two pulses. The polarization of the split pump pulses is rotated by passing them through a half-wave plate to 45° linear polarization with respect to the horizontal H (vertical V) basis defined by the polarization beam splitter (PBS) at the input (output) of the microstructure fiber. A transmission grating in the pump path directs the pump to a microstructure-fiber Sagnac interferometer composed of a PBS and a 1.8 m-long polarization-maintaining microstructure fiber. The fiber is twisted by 90° from end to end to have its principal axis oriented horizontally at one end and vertically at the other end, with the two ends facing the transmitting and reflecting ports of the PBS, respectively. Upon hitting the PBS, the first pump pulse splits into two equal-amplitude orthogonally polarized counterpropagating pulses. As a result of the built-in 90°-twist of the fiber, the counterpropagating pump pulses propagate along the same fiber eigenaxis, driving two identical FWM processes inside the fiber. We denote the transmitted pump H_p and the reflected pump V_p. H_p (V_p) probabilistically scatters copolarized FWM photon pairs $|H_sH_i\rangle$ ($|V_sV_i\rangle$), which copropagate with H_p (V_p) and become $|V_sV_i\rangle$ ($|H_sH_i\rangle$) at the output of the microstructure fiber due to its twist. The two orthogonally polarized FWM amplitudes are then recombined at the PBS into the same spatiotemporal mode to generate the polarization-entangled state $|H_sH_i\rangle+|V_sV_i\rangle$ in the first time slot ($|0\rangle$). The wave function of the two-photon state generated by the first pump pulse can therefore be written as

$$|\Psi\rangle_{p1} = (|H_sH_i\rangle + |V_sV_i\rangle) \otimes |0_s0_i\rangle, \tag{1}$$

where ⊗ stands for the direct product. The second pump pulse, which is delayed from the first pump pulse by $\Delta\tau$, undergoes exactly the same FWM process through the microstructure-fiber Sagnac interferometer, producing the same polarization entangled state (up to a fixed global phase) in the second time slot ($|1\rangle$). Similar to Eq. (1), the two-photon wave function generated by the second pump pulse is given by

$$|\Psi\rangle_{p2} = (|H_sH_i\rangle + |V_sV_i\rangle) \otimes |1_s1_i\rangle. \tag{2}$$

In the limit of low photon-scattering efficiency, in which case there is at most one pair of photons generated among the two consecutive time slots, the two polarization-entangled states, Eq. (1) and Eq. (2), must be coherently summed to give the desired hyperentangled state

$$|\Psi\rangle_{hyper} = (|H_sH_i\rangle + |V_sV_i\rangle) \otimes (|0_s0_i\rangle + |1_s1_i\rangle). \tag{3}$$

The generated broadband hyperentanglement is separated from the pump light by passing the output of the Sagnac interferometer through a double-pass grating filter, which is conveniently composed of the input pump grating and two mirrors with slits in front in a retroreflective configuration (see Fig. 1). This configuration uses the wavelength-filtering function of the grating twice, and allows flexible spectral tuning without affecting the optical alignment. In particular, the slits in front of the mirrors are placed on translation stages, so that their positions can be scanned during the experiment to find the energy-matching signal-idler photon pairs. The slit widths can also be tuned to select the desired bandwidth of the collected photons. For our current experiment, the central wavelength of the signal (idler) photon is chosen to be λ_s=689.9 nm (λ_i=799.6 nm) with $\Delta\lambda$ =0.9 nm, where the two-photon FWM gain is high and the single-photon noise background produced mainly by spontaneous Raman scattering is low. A broadband interference filter is placed in the signal (idler) photon's path to aid in achieving enough pump isolation (≈100 dB).

To analyze the degree of hyperentanglement for the generated state $|\Psi\rangle_{hyper}$, the signal and idler photons each pass through two cascaded analyzers (one for time bin and one for polarization), as shown in Fig. 1. The time-bin analyzer is just a polarization Michelson interferometer (PMI), which is composed of a PBS, two quarter-wave plates, and two mirrors. The path-length difference of the two signal PMI arms is set to exactly match that of the pump Michelson interferometer, corresponding to an optical delay of $\Delta\tau$=57 ps. The time-bin analyzer for the idler arm is constructed in an analogous fashion to the signal PMI with the same arm-length difference. In this way, the initial two time bins ($|0\rangle$ and $|1\rangle$) of the hyperentangled state $|\Psi\rangle_{hyper}$ are converted to three time bins $|0\rangle_a$, $|1\rangle_a$, and $|2\rangle_a$, where the subscript "a" denotes "after" the time-bin analyzers), with the central time bin ($|1\rangle_a$) containing the maximum overlap of the $|V_sV_i\rangle$ amplitude from the $|0\rangle$ time bin and the $|H_sH_i\rangle$ amplitude from the $|1\rangle$ time bin. The details of the time-bin analyzers are shown in Fig. 2. With redefined time bins $|0\rangle_a$, $|1\rangle_a$, and $|2\rangle_a$ (shown

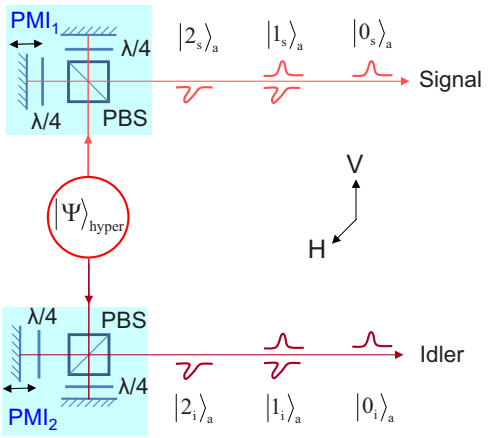

FIG. 2. (Color online) A schematic of the time-bin analyzers, which transform the two time bins of the original hyperentangled state ($|\Psi\rangle_{\text{hyper}}$) into three time bins ($|0\rangle_a$, $|1\rangle_a$, and $|2\rangle_a$), with the central time bin ($|1\rangle_a$) containing the overlapped FWM amplitudes. λ/4, quarter-wave plate; PBS, polarization beam splitter; PMI, polarization Michelson interferometer.

in Fig. 2), the horizontally polarized component of the incident $|\Psi\rangle_{\text{hyper}}$ state passes through the time-bin analyzers' short arms, and is transformed to

$$|H_sH_i\rangle \otimes (|0_s0_i\rangle + |1_s1_i\rangle) \rightarrow |V_sV_i\rangle \otimes (|0_s0_i\rangle_a + |1_s1_i\rangle_a). \tag{4}$$

The polarization flipping ($|H\rangle \rightarrow |V\rangle$) in Eq. (4) is due to the fact that the quarter-wave plates in the PMIs are oriented at 45°, so that a double pass through the quarter-wave plates rotates the incident light polarization by 90°. The vertically polarized component of $|\Psi\rangle_{\text{hyper}}$ is delayed by the time-bin analyzers' long arms to become

$$|V_sV_i\rangle \otimes (|0_s0_i\rangle + |1_s1_i\rangle) \rightarrow e^{i\phi}|H_sH_i\rangle \otimes (|1_s1_i\rangle_a + |2_s2_i\rangle_a), \tag{5}$$

where the relative phase ϕ can be tuned by scanning the PMIs' long arms while keeping their short arms fixed. This is achieved in the experiment by moving the mirrors in the time-bin analyzers' long arms using piezoelectric transducers (PZTs). It is worth noting that since ϕ is a collective phase from both PMIs' arm-length differences (i.e., $\phi = \phi_{\text{PMI}_1} + \phi_{\text{PMI}_2}$), it is equivalent to scan either PMI's long arm.

Equations (4) and (5), when combined, give the complete wave function of the two-photon state upon exiting the time-bin analyzers:

$$|\Phi\rangle \propto |V_sV_i\rangle \otimes |0_s0_i\rangle_a + (|V_sV_i\rangle + e^{i\phi}|H_sH_i\rangle) \otimes |1_s1_i\rangle_a + e^{i\phi}|H_sH_i\rangle \otimes |2_s2_i\rangle_a, \tag{6}$$

where an overall normalization factor is neglected. This state clearly exhibits polarization entanglement in the central time bin ($|1_s1_i\rangle_a$), which is inherited from the time-bin entanglement of its parent state $|\Psi\rangle_{\text{hyper}}$.

After going through the time-bin analyzers, the signal and idler photons each pass through a polarization analyzer in its own path, which consists of a half-wave plate and a PBS used to project the wave function to any desired linear polarization basis. The photons are finally detected in coincidence by two silicon avalanche single-photon detectors in a start-stop configuration, with the detection pulses from the signal (idler) acting as the start (stop).

We have done two sets of experiments to confirm the hyperentangled nature of the generated state $|\Psi\rangle_{\text{hyper}}$. In the first experiment, we set both polarization analyzers to be in the 45° linear polarization basis (i.e., $|D\rangle \equiv |H\rangle + |V\rangle$), and vary ϕ by applying a stepwise voltage on the PZT in the signal PMI. The theoretical total two-photon coincidence probability is given by

$$C_{\text{total}}^{\text{theory}} \propto |\langle D_sD_i|\Phi\rangle|^2 \propto 2 + 2(1 + \cos\phi). \tag{7}$$

The sinusoidal dependence of the total coincidence probability on ϕ is a manifestation of the inherent time-bin entanglement in $|\Psi\rangle_{\text{hyper}}$. The coincidence rate of interest, denoted as C_{hyper}, should be the coincidence only between the central overlapped time bins $|1_s\rangle_a$ and $|1_i\rangle_a$. In principle, C_{hyper} can be measured by using fast detectors with a response time shorter than $\Delta\tau = 57$ ps, the time separation between the three consecutive time bins. In practice, however, both single-photon detectors have much longer response times (on the order of 1 ns) than $\Delta\tau$, making it impossible to directly single out C_{hyper} from the experimentally measured $C_{\text{total}} = C_{\text{total}}^{\text{theory}} + A$, where A is the measured total accidental coincidence rate. Nevertheless, one can derive C_{hyper} using the following method. We equalize the four two-photon coincidence amplitudes ($|V_sV_i\rangle \otimes |0_s0_i\rangle_a$, $|V_sV_i\rangle \otimes |1_s1_i\rangle_a$, $|H_sH_i\rangle \otimes |1_s1_i\rangle_a$, and $|H_sH_i\rangle \otimes |2_s2_i\rangle_a$) that constitute $|\Phi\rangle$ by equalizing their corresponding coincidence rates (C_{V0}, C_{V1}, C_{H1}, and C_{H2}). As a result, the accidental coincidence rates among any pair of the above four two-photon amplitudes are also made equal. With help from Fig. 2, it can be seen that out of all 16 possible accidental coincidence rates, only 4 of them are entirely caused by the central time-bin amplitudes. In particular, these "accidental coincidence rates of interest" are accidental coincidences between $|V_s\rangle \otimes |1_s\rangle_a$ and $|V_i\rangle \otimes |1_i\rangle_a$, $|V_s\rangle \otimes |1_s\rangle_a$and $|H_i\rangle \otimes |1_i\rangle_a$, $|H_s\rangle \otimes |1_s\rangle_a$ and $|V_i\rangle \otimes |1_i\rangle_a$, and $|H_s\rangle \otimes |1_s\rangle_a$ and $|H_i\rangle \otimes |1_i\rangle_a$. The other 12 accidental coincidences are not exclusively related to the central time-bin amplitudes, and should be excluded from C_{total} to obtain C_{hyper}. The same strategy applies to C_{V0} and C_{H2}. In the end, C_{hyper} is obtained from the following formula:

$$C_{\text{hyper}} = C_{\text{total}} - C_{V0} - C_{H2} - \frac{3}{4}A. \tag{8}$$

The expected two-photon interference (TPI) is observed in C_{total} as shown in Fig. 3(a), where a total average pump power of 220 μW is used. C_{hyper} is obtained from Eq. (8), and is shown in Fig. 3(b). The subtracted terms (C_{V0}, C_{H2}, and A) have no dependence on ϕ, and were measured for a few representative values of ϕ. The TPI visibility for C_{hyper} [defined as (Max−Min)/(Max+Min) from the best sinusoidal fit to the data] is 88% ± 2%, which should be regarded as the raw visibility of time-bin entanglement since we have not subtracted the accidental coincidences entirely due to the central time bin $|1_s1_i\rangle_a$. Note that if we subtracted

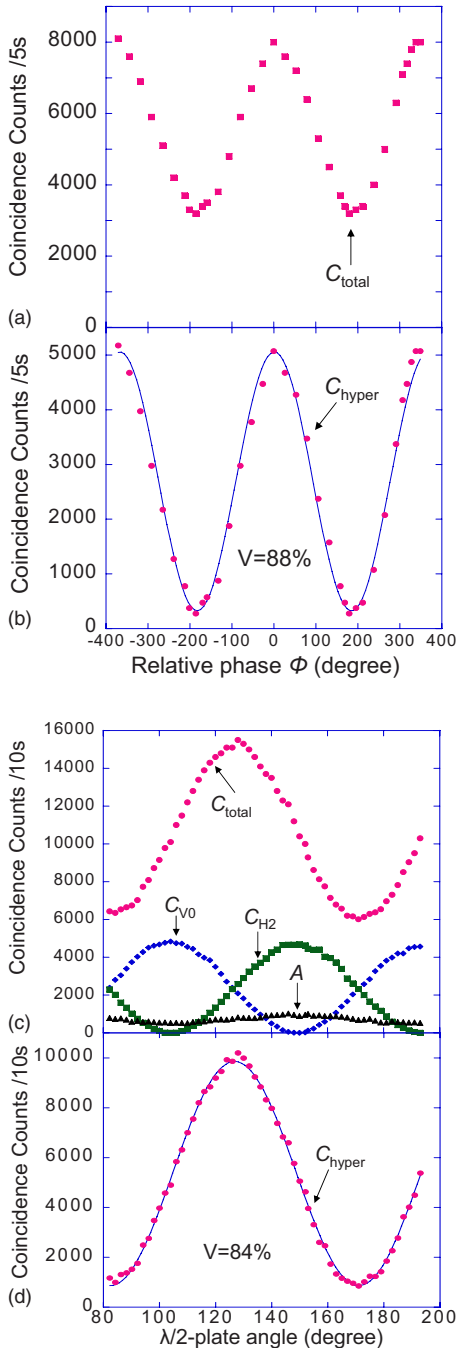

FIG. 3. (Color online) (a) Total coincidence rate C_{total} plotted as a function of the relative phase ϕ. (b) Time-bin TPI raw visibility ≈88%. (c) Total coincidence rate C_{total}, coincidence rates C_{V0} and C_{H2}, and accidental coincidence rate A plotted against the half-wave plate angle in the polarization analyzer in the signal's path. (d) Polarization TPI raw visibility ≈84%. Data are represented by solid dots, diamonds, squares, and triangles. The curves in (b) and (d) are sinusoidal fits to the TPI. *V*, visibility; TPI, two-photon interference.

the central time-bin accidental coincidences, the TPI visibility would become $91\% \pm 2\%$.

In the second experiment, we set the time-bin analyzers in both arms to be optimally overlapped for the central time bin [i.e., by setting $\phi=0$ in Eq. (6)], and scanned the half-wave plate in one of the polarization analyzers. The resulting TPI for C_{total} is shown in Fig. 3(c), together with the interference fringes for C_{V0}, C_{H2}, and A. Note that A is almost independent of the half-wave plate setting; its slight sinusoidal change is mainly due to the imperfectly balanced FWM amplitudes in Eq. (6). We then derive C_{hyper} using Eq. (8), and obtain a raw TPI visibility of $84\% \pm 1\%$, which is plotted in Fig. 3(d). The background-subtracted TPI visibility is $87\% \pm 1\%$ for this experiment. Since the time-bin and polarization TPI visibilities are both greater than $1/\sqrt{2}$, we conclude that the produced two-photon state $|\Psi\rangle_{hyper}$ is hyperentangled in both time-bin and polarization. All of the above results are obtained with a coincidence rate of ≈1 kHz.

With the produced Bell state in the second experiment in the central time bin $(|H_s H_i\rangle + |V_s V_i\rangle) \otimes |1_s 1_i\rangle_a$, we examined the Bell's inequality in its Clauser-Horne-Shimony-Holt form [26]. After completing a set of 16 twofold coincidence measurements in 16×10 s, we obtained $S=2.486 \pm 0.018$ (1σ) without subtraction of central-time-bin accidental coincidences [i.e., the only accidental coincidences subtracted were those appearing in Eq. (8)]. This shows an unambiguous violation of the classical limit of $S=2$ by 27 standard deviations.

The above TPI visibilities, although high enough to guarantee the existence of entanglement in both degrees of freedom, may appear reduced when compared with that from our previous work [17]. This can be mainly attributed to the apparently more complicated nature of the current experiment. Compared with Ref. [17], three more Michelson interferometers have been added in our current experiment to create and subsequently analyze time-bin entanglement. The entire hyperentanglement setup can thus be seen as a large interferometric system, requiring long-term stable overlapping between interfering FWM modes to obtain high TPI visibility. The long path length (≃5 m in free space) of each individual FWM mode (as shown in Fig. 2) as well as the smallness of the microstructure-fiber core (core diameter ≃1 μm) contribute to the major difficulties in maintaining stable alignment for the entire interferometric system. However, both obstacles are only technical in nature, and can be remedied by either shortening the path for each interfering FWM mode, or adopting a microstructure fiber that is tapered to a larger core size at the fiber ends, or a combination of both.

In conclusion, we have demonstrated the production of photon pairs hyperentangled in the time-bin and polarization degrees of freedom using four-wave mixing in a microstructure-fiber Sagnac interferometer. The high spectral brightness, wide wavelength tunability, and single-spatial-mode output make our source a promising candidate for use in many quantum-information-processing protocols, especially those which would benefit from photon pairs simultaneously entangled in more than one degree of freedom [4,27–29].

This work has been supported in part by the Intelligence Advanced Research Projects Activity (IARPA) Polarization-Entangled Photon Source Program, and the Multidisciplinary University Research Initiative Center for Photonic Quantum Information Systems (Army Research Office/IARPA Program No. DAAD19-03-1-0199). M.D.E. acknowledges support from the National Research Council.

[1] D. V. Strekalov, T. B. Pittman, A. V. Sergienko, Y. H. Shih, and P. G. Kwiat, Phys. Rev. A **54**, R1 (1996).
[2] T. Yang, Q. Zhang, J. Zhang, J. Yin, Z. Zhao, M. Żukowski, Z.-B. Chen, and J.-W. Pan, Phys. Rev. Lett. **95**, 240406 (2005).
[3] J. T. Barreiro, N. K. Langford, N. A. Peters, and P. G. Kwiat, Phys. Rev. Lett. **95**, 260501 (2005).
[4] M. Barbieri, F. De Martini, P. Mataloni, G. Vallone, and A. Cabello, Phys. Rev. Lett. **97**, 140407 (2006).
[5] P. G. Kwiat, J. Mod. Opt. **44**, 2173 (1997).
[6] P. G. Kwiat and H. Weinfurter, Phys. Rev. A **58**, R2623 (1998).
[7] *Technologies for Quantum Communications*, special issue of J. Mod. Opt. **48** (13) (2001).
[8] P. S. J. Russell, J. Lightwave Technol. **24** (12), 4729 (2006).
[9] J. E. Sharping, J. Chen, X. Li, P. Kumar, and R. S. Windeler, Opt. Express **12**, 3086 (2004).
[10] J. Fan, A. Dogariu, and L. J. Wang, Opt. Lett. **30**, 1530 (2005).
[11] O. Alibart, J. Fulconis, G. K. L. Wong, S. G. Murdoch, W. J. Wadsworth, and J. G. Rarity, New J. Phys. **8**, 67 (2006).
[12] M. Fiorentino, P. L. Voss, J. E. Sharping, and P. Kumar, IEEE Photon. Technol. Lett. **14**, 983 (2002).
[13] X. Li, P. L. Voss, J. E. Sharping, and P. Kumar, Phys. Rev. Lett. **94**, 053601 (2005).
[14] H. Takesue and K. Inoue, Phys. Rev. A **70**, 031802(R) (2004).
[15] K. F. Lee, J. Chen, C. Liang, X. Li, P. L. Voss, and P. Kumar, Opt. Lett. **31**, 1905 (2006).
[16] J. Chen, K. F. Lee, X. Li, P. L. Voss, and P. Kumar, New J. Phys. **9**, 289 (2007).
[17] J. Fan, M. D. Eisaman, and A. Migdall, Phys. Rev. A **76**, 043836 (2007).
[18] J. Fulconis, O. Alibart, J. L. O'Brien, W. J. Wadsworth, and J. G. Rarity, e-print arXiv:quant-ph/0611232.
[19] H. Takesue and K. Inoue, Opt. Express **13**, 7832 (2005).
[20] J. Brendel, N. Gisin, W. Tittel, and H. Zbinden, Phys. Rev. Lett. **82**, 2594 (1999).
[21] J. D. Franson, Phys. Rev. Lett. **62**, 2205 (1989).
[22] I. Marcikic, H. de Riedmatten, W. Tittel, H. Zbinden, M. Legré, and N. Gisin, Phys. Rev. Lett. **93**, 180502 (2004).
[23] H. Takesue, Opt. Express **14**, 3453 (2006).
[24] F. Bussières, Y. Soudagar, G. Berlin, S. Lacroix, and N. Godbout, e-print arXiv:quant-ph/0605066.
[25] G. P. Agrawal, *Nonlinear Fiber Optics* (Academic, San Diego, 2001).
[26] J. F. Clauser, M. A. Horne, A. Shimony, and R. A. Holt, Phys. Rev. Lett. **23**, 880 (1969).
[27] C. Simon and J.-W. Pan, Phys. Rev. Lett. **89**, 257901 (2002).
[28] C. Wang, F.-G. Deng, Y.-S. Li, X.-S. Liu, and G. L. Long, Phys. Rev. A **71**, 044305 (2005).
[29] N. J. Cerf, M. Bourennane, A. Karlsson, and N. Gisin, Phys. Rev. Lett. **88**, 127902 (2002).